

# Role of MgO barriers for spin and charge transport in Co/MgO/graphene non-local spin-valve devices

F. Volmer, M. Drögeler, E. Maynicke, N. von den Driesch, M. L. Boschen, G. Güntherodt, and B. Beschoten\*

*II. Institute of Physics, RWTH Aachen University, 52056 Aachen, Germany and JARA-Fundamentals of Future Information Technology, Jülich-Aachen Research Alliance, Germany*

(Dated: April 14, 2019)

We investigate spin and charge transport in both single and bilayer graphene non-local spin-valve devices. Similar to previous studies on bilayer graphene, we observe an inverse dependence of the spin lifetime on the carrier mobility in our single layer devices. This general trend is only observed in devices with large contact resistances ( $> 1 \text{ k}\Omega$ ). Furthermore, we observe a second Dirac peak in devices with long spin lifetimes. This results from charge transport underneath the contacts. In contrast, all devices with low ohmic contact resistances only exhibit a single Dirac peak. Additionally, the spin lifetime is significantly reduced indicating that an additional spin dephasing occurs underneath the electrodes.

Graphene has drawn strong attention because of spin lifetimes up to the ns regime and spin diffusion lengths of some  $\mu\text{m}$  at room temperature.<sup>1–11</sup> Nevertheless, the experimental values of the spin lifetimes are some orders of magnitude shorter than theoretically predicted<sup>12,13</sup> indicating that in present devices spin transport is limited by extrinsic sources of spin scattering. These include spin-orbit coupling by adatoms, edge effects and ripples.<sup>8,12,14–18</sup> Additionally, spin scattering may result from the underlying substrate or the spin injection and detection contacts.<sup>13,19,20</sup> The importance of the latter might be indicated by recent electron spin resonance (ESR) experiments on graphene nanoribbons and small flakes that were only weakly coupled to the substrate and had no electrodes.<sup>21,22</sup> Interestingly, the measured spin lifetimes of localized spin states are at least 200 ns while the estimated spin lifetimes of conduction electrons are 30 ns, which is larger than any reported values from Hanle spin precession measurements in spin transport.

In this Rapid Communication, we investigate the influence of MgO barriers on spin and charge transport properties by fabricating both single layer (SLG) and bilayer graphene (BLG) non-local spin-valve devices with both low ohmic (transparent) and high resistive MgO/Co contacts. We explore the relationship between spin lifetime and charge carrier mobility in SLG and find a similar  $1/\mu$  dependence as seen in previous spin transport studies on exfoliated bilayer graphene (BLG) devices.<sup>5</sup> This dependence is only observed in samples with large contact resistances. In fact, we observe that devices with long spin lifetimes additionally exhibit a second Dirac peak in charge transport, which stems from the electrodes. We observe that this contact-induced Dirac peak overlaps with the Dirac peak of the bare graphene which complicates the analysis of the carrier mobility and thus complicates a clear assignment of the dominant spin scattering mechanism in graphene. For devices with low contact resistances we find an overall strong decrease of the spin lifetime showing that transparent contacts yield additional spin dephasing in graphene underneath the electrodes.

We have fabricated exfoliated SLG and BLG devices

on  $\text{SiO}_2(300 \text{ nm})/\text{Si}^{++}$  wafers. The number of graphene layers is determined by optical contrast measurement which is calibrated by Raman spectroscopy. After e-beam lithography we use molecular beam epitaxy to first grow an MgO spin injection/detection barrier with varying thicknesses from 1 nm up to 3 nm followed by 35 nm thick ferromagnetic Co contacts. The rather thick barrier is necessary due to the fact that MgO on graphene grows in the Volmer-Weber mode (island formation) if no wetting layer is used.<sup>23</sup> We have evidence that even devices with high resistive contacts that show non-linear differential I-V-curves still exhibit pinholes in the barrier.<sup>24</sup>

All transport measurements are performed under vacuum condition at room temperature using standard lock-in techniques.<sup>25</sup> The highly doped  $\text{Si}^{++}$ -wafer is used as a backgate which allows changing the charge carrier density  $n = \alpha(V_G - V_D)$  in the graphene sheet according to the established capacitor model<sup>26</sup> with  $\alpha \approx 7.18 \cdot 10^{10} \text{ V}^{-1}\text{cm}^{-2}$ ,  $V_G$  being the applied gate voltage and  $V_D$  being the gate voltage position of the maximum resistivity at the charge neutrality point, also called Dirac point. By a linear fit of the conductance  $\sigma$ , we extract the charge carrier mobility  $\mu = 1/e \cdot \partial\sigma/\partial n$  at an electron density of  $n = 1.5 \cdot 10^{12} \text{ cm}^{-2}$ . Hanle spin precession measurements are performed in standard non-local 4-terminal geometry and are fitted by a simplified analytical solution<sup>27,28</sup> of the steady-state Bloch-Torrey equation:<sup>25</sup>

$$\frac{\partial \vec{s}}{\partial t} = \vec{s} \times \vec{\omega}_0 + D_s \nabla^2 \vec{s} - \frac{\vec{s}}{\tau_s} = 0, \quad (1)$$

where  $\vec{s}$  is the net spin vector,  $\omega_0 = g\mu_B B/\hbar$  the Larmor frequency,  $D_s$  the spin diffusion constant and  $\tau_s$  the transverse spin lifetime. Recent experiments indicate that the effective g-factor in graphene-based spin transport devices may differ from the free electron value at low temperatures after a hydrogen treatment.<sup>29</sup> As ESR measurements for untreated graphene show  $g \approx 2$  even for low temperatures<sup>21,22</sup> and we also restrict ourselves to room temperature (RT) analysis in the present study, we assume  $g = 2$  for all devices.

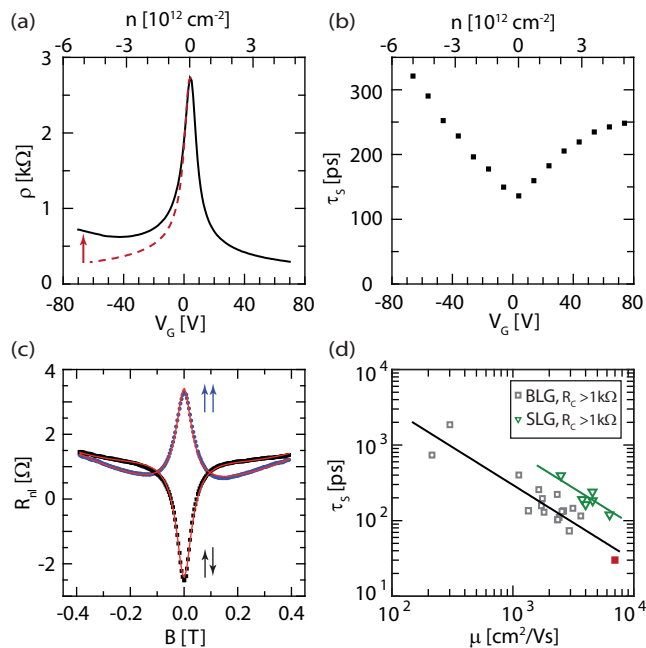


Figure 1. (Color online) (a) Gate dependent resistivity of a SLG device with large contact resistance. The resistivity increase towards negative  $V_G$  (see red arrow) indicates the existence of a second charge neutrality point. As a guide to the eye the electron branch for  $V_G > 0$  is mirrored at the Dirac point (red dashed line). (b)  $\tau_s$  vs  $V_G$  and  $n$ ; the minimum at the Dirac point is typical for devices with large contact resistances. (c) Hanle spin precession measurement for a magnetic field perpendicular to the plane. The arrows indicate the relative orientation of the magnetization directions of injection and detection electrode. (d)  $\tau_s$  vs  $\mu$  at  $n = 1.5 \cdot 10^{12} \text{ cm}^{-2}$  taken at RT for BLG (taken from Ref. 5) and SLG devices with high resistive contacts. The lines are the best fit to a DP like spin dephasing. The BLG device with the shortest spin lifetime (filled square) will be discussed separately in the text.

In Figs. 1(a)-(c) we show typical transport data for a SLG device with large contact resistances  $R_C > 1 \text{ k}\Omega$ .<sup>25</sup> We first note that there is a strong electron-hole asymmetry in charge transport (Fig. 1(a)) as seen by the increase of the graphene resistivity for hole doping towards large negative  $V_G$  values. Its origin will be discussed further below. Spin lifetimes are extracted from Hanle curves, which have been measured in perpendicular magnetic fields for both parallel and antiparallel alignments of the respective magnetization directions of neighboring Co electrodes (Fig.1(c)). The gate voltage dependent  $\tau_s$  times in Fig. 1(b) show a minimum at the Dirac point and strongly increase with both electron and hole doping. This general trend is observed for most large  $R_C$  devices.

We next evaluate the dependence of  $\tau_s$  on the electron mobility  $\mu$  at  $n = 1.5 \cdot 10^{12} \text{ cm}^{-2}$  for all SLG devices in Fig. 1(d) (green triangles) on a log-log scale. For easier comparison we include results on BLG (black squares in Fig. 1(d)), which some of us had previously mea-

sured.<sup>5</sup> The most striking observation is that like in BLG  $\tau_s$  depends inversely on  $\mu$  in our SLG devices. This relationship was previously attributed to the dominance of D'yakonov-Perel' (DP) like spin dephasing in graphene.

Remarkably, SLG devices exhibit longer spin lifetimes than BLG devices of equal mobility. The vertical offset between SLG and BLG in Fig. 1(d) can be analyzed within the DP spin dephasing mechanism. For this we replace the momentum scattering time  $\tau_m$  in the DP formula  $1/\tau_s = \Omega_{\text{eff}}^2 (\Delta_{\text{SO}}) \tau_m$ <sup>27</sup> with the Boltzmann expression of the mobility  $\mu = e\tau_m/m_{\text{eff}}^*$  and take the logarithm:

$$\ln(\tau_s) = \ln\left(\frac{e}{\Omega_{\text{eff}}^2 (\Delta_{\text{SO}}) \cdot m_{\text{eff}}^*}\right) - \ln(\mu), \quad (2)$$

where  $e$  is the elementary charge,  $\Omega_{\text{eff}}^2$  the effective Larmor frequency which is dependent on the spin-orbit coupling  $\Delta_{\text{SO}}$  and  $m_{\text{eff}}^*$  is the effective mass. With this expression it is obvious that the vertical offset in Fig. 1(d) can either result from a smaller effective mass or a smaller overall spin-orbit coupling strength in the SLG devices. We note that SLG is expected to exhibit massless Dirac fermions near the Dirac point only in simple tight-binding approximations. It has been shown that even the small intrinsic spin-orbit coupling in SLG gives rise to a small effective mass of the charge carriers,<sup>30,31</sup> which supports our simple approach in Eq. 2. Even stronger effects are expected from extrinsic sources such as contacts, adatoms, and the underlying substrate.<sup>13,16,17</sup> As all experimental values of  $\tau_s$  are well below theoretical predictions, we expect that spin relaxation and dephasing is governed by extrinsic sources in present devices. Because of the dominant extrinsic contribution to the spin-orbit coupling slight changes in the fabrication steps between the BLG and SLG devices (another batch of wafer, another resist for lithography) might be the reason for the observed offset in the lifetime. We note that changes in the sample fabrication may also lead to overall larger carrier mobilities in the new series of SLG devices.

In the following, we will focus on the influence of the contact resistance on the measured spin lifetime. Several groups have suggested to use high resistive tunneling contacts to avoid the backflow of charge carrier spins into the ferromagnetic electrodes which otherwise yields a reduction of the spin lifetime.<sup>3,19,20,32</sup> As mentioned above, all of our SLG devices exhibit large contact resistances  $R_c$ . Revisiting our previous BLG measurements also reveals  $R_c$  values above  $1 \text{ k}\Omega$  for almost all BLG data points in Fig. 1(d) (black squares). We note that there is no systematic dependence of  $\tau_s$  on  $R_c$ . Only the BLG device with the highest mobility (red, filled square in Fig. 1(d)) has low ohmic, transparent contacts with a flat differential  $dI/dV$ -curve.<sup>25</sup>

At first sight this sample seems to follow the DP like trend of the high resistive BLG devices. To explore this in further detail we fabricated additional SLG and BLG samples with in total 14 devices with a thinner MgO barrier but otherwise same fabrication procedure. Most of those show four-probe contact resistances well under

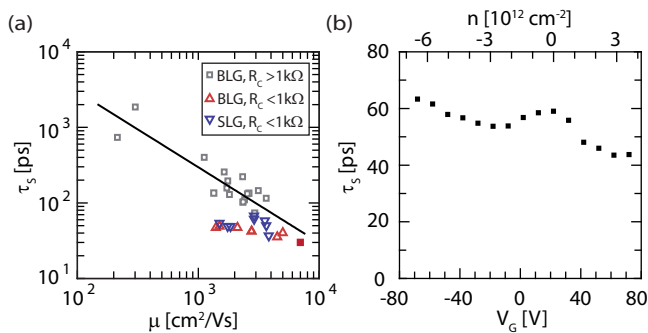


Figure 2. (Color online) (a) Spin lifetime  $\tau_s$  vs electron mobility  $\mu$  taken at an electron density of  $n = 1.5 \cdot 10^{12} \text{ cm}^{-2}$  at 300 K. Squares are taken from Ref. 5; upward and downward pointing triangles are BLG and SLG devices, respectively. Both exhibit low contact resistances  $R_c < 1 \text{ k}\Omega$ . (b) Typical gate voltage dependent spin lifetime for a device with transparent contacts.

200  $\Omega$  for electrode widths varying between 300 – 600 nm and graphene flake widths between 1 – 3  $\mu\text{m}$ . As seen in Fig. 2(a), all of those devices (upward pointing triangles for BLG and downward pointing ones for SLG) exhibit strongly reduced spin lifetimes which vary between 30 and 70 ps and lie well below all large  $R_c$  samples with no significant difference between SLG and BLG devices. Furthermore, the data do not follow the  $1/\mu$  dependence. It is therefore obvious that devices with low ohmic contact resistances exhibit short spin lifetimes which likely arises from spin dephasing underneath the contact area, e.g., by a partial backflow of the injected spin accumulation across the injection barrier during lateral diffusion.

The strong influence of low  $R_c$  contacts on the spin transport can also be seen by the charge density dependence of  $\tau_s$  (Fig. 2(b)), which is similar for all low  $R_c$  devices. In contrast to all large  $R_c$  devices (see Fig. 1(b)),  $\tau_s$  does not increase away from the Dirac point, but it rather decreases and may increase again at larger carrier densities. Although we presently do not understand this qualitative change in the density dependence, we note that such a decrease of  $\tau_s$  has previously been observed in BLG at low temperatures with large  $R_c$  contacts.<sup>5</sup>

Another intriguing difference between low and large  $R_c$  devices becomes evident in charge transport. While there is one Dirac peak around zero gate voltage in all low  $R_c$  devices (see Fig. 3(c)), we typically observe a second Dirac peak at larger negative gate voltages for SLG and BLG devices with large  $R_c$  exhibiting long spin lifetimes (Figs. 3(a) and (b)). Such a second Dirac peak is already observed in spin-valve devices by another group.<sup>33</sup> The resistivity ratio of both Dirac peaks varies significantly from device to device. Not all large  $R_c$  devices show the maximum of the second Dirac peak for  $V_G > -80 \text{ V}$  (cp. to Fig. 1(a)). But the general trend is that the separation between both Dirac peaks gets smaller for devices with longer spin lifetimes. Consistent with this the smallest peak separation has been observed in the device with the

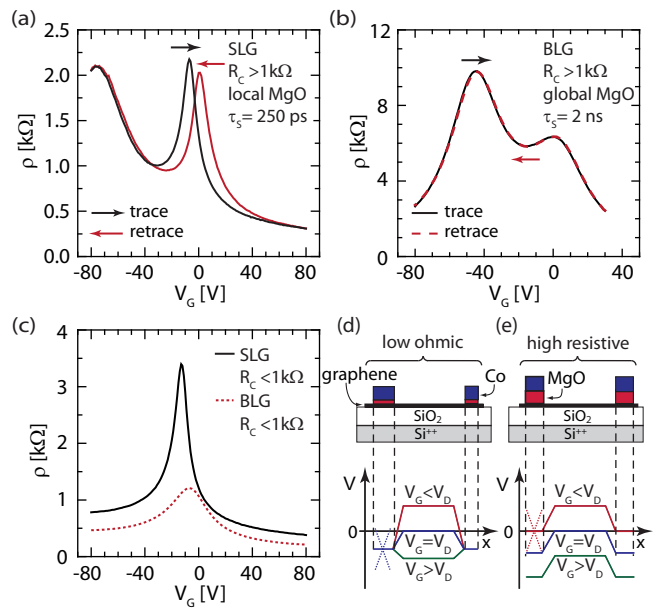


Figure 3. (Color online) (a) Gate voltage dependent resistivity of a high resistive SLG device with  $\tau_s = 250 \text{ ps}$  showing a pronounced contact-induced second Dirac peak at  $V_G = -75 \text{ V}$ . This Dirac peak does not show any hysteresis in contrast to the Dirac peak of the bare graphene near  $V_G = 0 \text{ V}$ . The arrows indicate the sweep directions of the gate voltage. (b)  $\rho$  vs  $V_G$  for a high resistive BLG device with  $\tau_s = 2 \text{ ns}$  (see Fig. 2(a)) and completely MgO covered graphene. No hysteresis is visible. (c)  $\rho$  vs  $V_G$  of SLG and BLG devices with low  $R_c$  contacts. Besides to a doping, the contacts may screen the gate field  $V_G$  which can result in (d) pinning (low  $R_c$ ) or (e) no pinning (high  $R_c$ ) of the electrostatic potential under the contacts (corresponding Dirac cones indicated).

longest  $\tau_s$  of 2 ns (Fig. 3(b)).

The left Dirac peak most likely results from the magnetic electrodes while the right Dirac peak is due to charge carrier transport through the graphene sheet between the electrodes. This notion is supported by hysteresis measurements when comparing different devices with local and global MgO barriers. In the former case MgO is only deposited underneath the ferromagnetic electrodes (see Fig. 3(a) for corresponding SLG device) while in the latter case MgO completely covers the graphene flake (see Fig. 3(b)). A hysteresis is only observed for the right Dirac peak in the device with local MgO barriers (Fig. 3(a)). It can originate from a thin water film on top of the graphene flake.<sup>34</sup> Although we measure under vacuum condition, such a hysteresis is initially always observed before the water will eventually evaporate after a few hours. However, no hysteresis for the left Dirac peak at negative gate voltages is observed. If this peak results from the contact area, this is also expected as water cannot cover the graphene underneath the contact area. Consistent with this assignment, we do not observe any hysteresis for global MgO devices (see

Fig. 3(b)).

We next focus on the origin of the left Dirac peak. It is well known that the contact material has a great influence on the transport properties in graphene. Scanning photocurrent microscopy experiments, for example, directly probe contact-induced doping and show Fermi level pinning from metallic electrodes.<sup>35</sup> A gate voltage dependent doping profile of the electrostatic potential  $V$  for devices with low ohmic contacts is depicted in Fig. 3(d). Here  $-e \cdot V$  equals to the position of the Fermi level in the graphene band structure. It has been argued that the Fermi level under the contacts is not affected by the gate voltage because the gate field is screened by the electrons spilling out from the metallic electrodes. Although this profile can successfully explain an electron-hole-asymmetry in the resistivity,<sup>36</sup> which we also observe in our low  $R_c$  devices, it cannot explain the second Dirac peak as the carrier density underneath the electrodes is not affected by the gate voltage.

In contrast, Nouchi *et al.*<sup>36</sup> have shown that charge density pinning by the contacts can be suppressed by oxidation of the electrodes which diminishes the screening of the gate field. This situation is illustrated in Fig. 3(e) where the gate voltage now also tunes the carrier density underneath the contacts. The two Dirac peaks thus yield different doping densities in the bare graphene and the graphene underneath the contacts at  $V_G = 0V$ , which results in a lateral p-n junction. This explanation is in agreement with our findings as the left Dirac peak is contact-induced and only visible in devices with large contact resistances. But it should be noted that the transition between pinning and depinning should in principal be continuous with increasing barrier thickness. That means that the appearance of the second Dirac peak does not necessarily imply a complete depinning. Considering the spatially inhomogeneous barrier thickness because of the Volmer-Weber growth mechanism and the most likely existing pinholes, we expect that our high resistive devices are in a transition state between pinning and complete depinning.

For the calculation of the electron mobilities and densities in Figs. 1(d) and 2(a) we have always used the right Dirac peak which we attribute to the bare graphene part. This might be a good approach for devices with only one Dirac peak (Fig. 3(c)) or for devices where the left Dirac peak is strongly separated in gate voltage as in Fig. 1(a).

In particular for devices with long spin lifetimes, however, the two Dirac peaks are not well separated but strongly overlap as seen in Figs. 3(a) and 3(b) for large  $R_c$  SLG and BLG devices, respectively. This overlapping has significant influence on the slope  $\partial\rho/\partial V_G$  of the right Dirac peak at  $n = 1.5 \cdot 10^{12} \text{ cm}^{-2}$  ( $V_G - V_D \approx 20 \text{ V}$ ). The smaller the separation between both Dirac peaks becomes the smaller the respective slope and carrier mobility will be. We note that this results in an underestimation of the mobility of the bare graphene part. It is important to emphasize that the contact-induced left Dirac peak might thus partially be responsible for the decrease in observed carrier mobility for devices with longer spin lifetimes.

There are more elaborated models to determine carrier mobilities including contact-induced pinning and depinning of the Fermi level and the respective potential profiles of the graphene along the device.<sup>33,37-40</sup> However, there are too many unknown quantities which currently hinder to extract reliable values for the respective carrier mobilities in the different graphene parts from a single gate dependent resistivity measurement.<sup>25</sup> Without further measurements of the potential profile we thus cannot give a more precise evaluation of the influence of the contact induced Dirac peak on the carrier mobility. This, on the other hand, would be important for identifying intrinsic spin dephasing mechanisms in graphene. Our findings show that the understanding of spin transport in graphene based non-local spin-valve devices requires independent understanding of both spin and charge transport properties which may significantly differ in graphene underneath the spin injection and detection electrodes and graphene between the electrodes.<sup>7</sup>

In summary, we have studied spin and charge transport in graphene-based non-local spin-valves by tuning the MgO injection/detection barrier from low ohmic to high resistive tunneling behavior. For low resistive contacts, there is a significant spin dephasing in graphene underneath the contacts, while SLG and BLG devices with large contact resistances show long spin lifetimes at room temperature. The latter devices exhibit a second Dirac peak at negative gate voltages. As the peak separation is smallest for devices with longest spin lifetimes, it might partially account for the observed  $1/\mu$  dependence of  $\tau_s$ .

This work was supported by DFG through FOR 912.

\* e-mail: bernd.beschoten@physik.rwth-aachen.de

<sup>1</sup> N. Tombros, C. Jozsa, M. Popinciuc, H. T. Jonkman, and B. J. van Wees, *Nature* **448**, 571 (2007).

<sup>2</sup> T. Maassen, J. J. van den Berg, N. IJbema, F. Fromm, T. Seyller, R. Yakimova, and B. J. van Wees, *Nano Letters* **12**, 1498 (2012).

<sup>3</sup> B. Dlubak, M.-B. Martin, C. Deranlot, B. Servet, S. Xavier, R. Mattana, M. Sprinkle, C. Berger, W. A. De Heer, F. Petroff, A. Anane, P. Seneor, and A. Fert,

*Nat Phys* **8**, 557 (2012).

<sup>4</sup> W. Han and R. K. Kawakami, *Phys. Rev. Lett.* **107**, 047207 (2011).

<sup>5</sup> T.-Y. Yang, J. Balakrishnan, F. Volmer, A. Avsar, M. Jaiswal, J. Samm, S. R. Ali, A. Pachoud, M. Zeng, M. Popinciuc, G. Güntherodt, B. Beschoten, and B. Özyilmaz, *Phys. Rev. Lett.* **107**, 047206 (2011).

<sup>6</sup> W. Han, J.-R. Chen, D. Wang, K. M. McCreary, H. Wen, A. G. Swartz, J. Shi, and R. K. Kawakami,

- Nano Letters **12**, 3443 (2012).
- <sup>7</sup> M. H. D. Guimaraes, A. Veligura, P. J. Zomer, T. Maassen, I. J. Vera-Marun, N. Tombros, and B. J. van Wees, Nano Letters **12**, 3512 (2012).
  - <sup>8</sup> A. G. Swartz, J.-R. Chen, K. M. McCreary, P. M. Odenthal, W. Han, and R. K. Kawakami, Phys. Rev. B **87**, 075455 (2013).
  - <sup>9</sup> B. Birkner, D. Pachniowski, A. Sandner, M. Ostler, T. Seyller, J. Fabian, M. Ciorga, D. Weiss, and J. Eroms, Phys. Rev. B **87**, 081405 (2013).
  - <sup>10</sup> S. Jo, D.-K. Ki, D. Jeong, H.-J. Lee, and S. Kettemann, Phys. Rev. B **84**, 075453 (2011).
  - <sup>11</sup> I. Neumann, J. Van de Vondel, G. Bridoux, M. V. Costache, F. Alzina, C. M. S. Torres, and S. O. Valenzuela, Small **9**, 156 (2013).
  - <sup>12</sup> D. Huertas-Hernando, F. Guinea, and A. Brataas, Phys. Rev. Lett. **103**, 146801 (2009).
  - <sup>13</sup> C. Ertler, S. Kunschuh, M. Gmitra, and J. Fabian, Phys. Rev. B **80**, 041405 (2009).
  - <sup>14</sup> M. Wojtaszek, I. J. Vera-Marun, T. Maassen, and B. J. van Wees, Phys. Rev. B **87**, 081402 (2013).
  - <sup>15</sup> K. Pi, W. Han, K. M. McCreary, A. G. Swartz, Y. Li, and R. K. Kawakami, Phys. Rev. Lett. **104**, 187201 (2010).
  - <sup>16</sup> A. H. Castro Neto and F. Guinea, Phys. Rev. Lett. **103**, 026804 (2009).
  - <sup>17</sup> P. Zhang and M. W. Wu, New Journal of Physics **14**, 033015 (2012).
  - <sup>18</sup> A. Avsar, T.-Y. Yang, S. Bae, J. Balakrishnan, F. Volmer, M. Jaiswal, Z. Yi, S. R. Ali, G. Guntherodt, B. H. Hong, B. Beschoten, and B. Ozyilmaz, Nano Letters **11**, 2363 (2011).
  - <sup>19</sup> W. Han, K. Pi, K. M. McCreary, Y. Li, J. J. I. Wong, A. G. Swartz, and R. K. Kawakami, Phys. Rev. Lett. **105**, 167202 (2010).
  - <sup>20</sup> T. Maassen, I. J. Vera-Marun, M. H. D. Guimarães, and B. J. van Wees, Phys. Rev. B **86**, 235408 (2012).
  - <sup>21</sup> S. S. Rao, A. Stesmans, J. van Tol, D. V. Kosynkin, A. Higginbotham-Duque, W. Lu, A. Sinitskii, and J. M. Tour, ACS Nano **6**, 7615 (2012).
  - <sup>22</sup> M. A. Augustyniak-Jablokow, K. Tadyszak, M. Mackowiak, and S. Lijewski, Chemical Physics Letters **557**, 118 (2013).
  - <sup>23</sup> W. H. Wang, W. Han, K. Pi, K. M. McCreary, F. Miao, W. Bao, C. N. Lau, and R. K. Kawakami, Applied Physics Letters **93**, 183107 (2008).
  - <sup>24</sup> Paper in preparation.
  - <sup>25</sup> See Supplemental Material for a more detailed description of device fabrication, measurement methods and supporting measurements.
  - <sup>26</sup> K. S. Novoselov, A. K. Geim, S. V. Morozov, D. Jiang, Y. Zhang, S. V. Dubonos, I. V. Grigorieva, and A. A. Firsov, Science **306**, 666 (2004).
  - <sup>27</sup> J. Fabian, A. Matos-Abiague, C. Ertler, P. Stano, and I. Zutic, ACTA PHYSICA SLOVACA **57**, 565 (2007).
  - <sup>28</sup> M. Johnson and R. H. Silsbee, Phys. Rev. B **37**, 5312 (1988).
  - <sup>29</sup> K. M. McCreary, A. G. Swartz, W. Han, J. Fabian, and R. K. Kawakami, Phys. Rev. Lett. **109**, 186604 (2012).
  - <sup>30</sup> M. Gmitra, S. Kunschuh, C. Ertler, C. Ambrosch-Draxl, and J. Fabian, Phys. Rev. B **80**, 235431 (2009).
  - <sup>31</sup> S. Kunschuh, M. Gmitra, and J. Fabian, Phys. Rev. B **82**, 245412 (2010).
  - <sup>32</sup> M. Popinciuc, C. Józsa, P. J. Zomer, N. Tombros, A. Veligura, H. T. Jonkman, and B. J. van Wees, Phys. Rev. B **80**, 214427 (2009).
  - <sup>33</sup> I. J. Vera-Marun, V. Ranjan, and B. J. van Wees, Nat Phys **8**, 313 (2012).
  - <sup>34</sup> H. Wang, Y. Wu, C. Cong, J. Shang, and T. Yu, ACS Nano **4**, 7221 (2010).
  - <sup>35</sup> T. Mueller, F. Xia, M. Freitag, J. Tsang, and P. Avouris, Phys. Rev. B **79**, 245430 (2009).
  - <sup>36</sup> R. Nouchi and K. Tanigaki, Applied Physics Letters **96**, 253503 (2010).
  - <sup>37</sup> S. A. Thiele, J. A. Schaefer, and F. Schwierz, Journal of Applied Physics **107**, 094505 (2010).
  - <sup>38</sup> D. Jimenez, Electron Devices, IEEE Transactions on **58**, 4377 (2011).
  - <sup>39</sup> R. Nouchi and K. Tanigaki, Japanese Journal of Applied Physics **50**, 070109 (2011).
  - <sup>40</sup> Q. Li, E. H. Hwang, E. Rossi, and S. Das Sarma, Phys. Rev. Lett. **107**, 156601 (2011).